In-depth study of the formation processes of single atmospheric particles in the southeastern margin of Tibetan Plateau

Li Li[1,3], Qiyuan Wang[1,2], Jie Tian[1], Huikun Liu[1], Yong Zhang[1], Steven Sai Hang Ho[4], Weikang Ran[1], Junji Cao[5]

[1] Key Laboratory of Aerosol Chemistry and Physics, State Key Laboratory of Loess and Quaternary Geology, Institute of Earth Environment, Chinese Academy of Sciences, Xi'an 710061, China
[2] CAS Center for Excellence in Quaternary Science and Global Change, Xi'an 710061, China
[3] University of Chinese Academy of Sciences, Beijing 100049, China
[4] Division of Atmospheric Sciences, Desert Research Institute, Reno, NV 89512, United States
[5] Institute of Atmospheric Physics, Chinese Academy of Sciences, Beijing 100029, China

Correspondence to: Qiyuan Wang (wangqy@ieecas.cn) and Junji Cao (jjcao@mail.iap.ac.cn).

Text S1. Characteristics of particle composition

Particles containing the strongest K^+ (*m/z* $^{39}K^+$) signal in the positive MS, significant sulfate (*m/z* $^{97}HSO_4^-$), and nitrate (*m/z* $^{46}NO_2^-$, $^{62}NO_3^-$) fragments in the negative MS are identified as Potassium-rich (rich-K) (Fig. S3a). The sources of the rich-K particles are complex, including biomass burning (Pratt et al., 2011), atmospheric aging (Bi et al., 2011; Shen et al., 2017), and industrial and traffic emissions (Zhang et al., 2017). A weak phosphate (*m/z* $^{79}PO_3^-$) signal can be seen in Fig. S3a, while a study supported that $^{79}PO_3^-$ could be originated from motor vehicle lubricants (Yang et al., 2017). Significant peaks of $^{97}HSO_4^-$ and $^{62}NO_3^-$ indicate that the rich-K particle might also experience atmospheric aging after the primary biomass burning emission (with Cluster 2 which will be discussed in Section 3.2). The particles containing levoglucosan fragments ($^{45}CHO_2^-$, $^{59}C_2H_3O_2^-$, $^{71}C_3H_3O_2^-$, $^{73}C_3HO_3^-$) and $^{113,115}K_2Cl^+$ signals in Fig. S3b are defined as Biomass Burning (BB) (Moffet et al., 2008). Organic carbon (OC) particles (Fig.S3c) have strong organic fragments (such as *m/z* $^{27}C_2H_3^+$, $^{37}C_3H^+$, $^{43}C_2H_3O^+$ and $^{51}C_4H_3^+$) in the positive MS, generally from biomass burning and VOCs transformation (Moffet et al., 2008; Bi et al., 2011). Strong $^{97}HSO_4^-$ and $^{62}NO_3^-$ signals in the negative MS represent that the particles have experienced a certain degree of aging in the atmosphere. In addition, $^{79}PO_3^-$ in the negative MS demonstrates the OC is also contributed by traffic emissions. However, the larger molecular weight ions (*m/z* −129, −143) contained in OC negative MS cannot be well interpreted, potentially ascribed to the presence of organo-sulfate (Hatch et al 2011; Cahill et al., 2012). Notably different from other types of particle, Ammonium particle contains apparent ammonium ions (*m/z* $^{18}NH_4^+$) and diethylamine (*m/z* $^{58}C_2H_5NHCH_2^+$) in the positive MS (Fig. S3d), and strong $^{97}HSO_4^-$ signals in the negative MS. The presence of sulfuric acid (*m/z* $^{195}H(HSO_4)_2^-$) fragments indicates that ammonium is an acidic particle (Rehbein et al., 2011; Lin et al., 2017). There are a variety of sources of ammonium, including sewage treatment, animal husbandry, waste incineration, the marine environment, biomass burning, industrial processes, and vehicle exhaust (Cadle and Mulawa, 1980; Moffet et al.,

2008). Moreover, its gaseous precursor of ammonia (NH_3) could be converted into secondary aerosols such as ammonium sulfate/nitrate (Seinfeld and Pandis, 2012; Yang et al., 2012). In this study, ammonium particles show negligible $^{62}NO_3^-$ fragment in the negative MS due to ammonium nitrate being much more volatile and less easily transported than ammonium sulfate (Lall and Thurston 2006; Sun et al. 2012; Xu et al., 2018). These results possibly suggest that ammonium particles have undergone intense atmospheric aging during regional transport. Element carbon (EC-aged) particles are characterized by the obvious signals of carbon cluster ions (e.g., *m/z* $^{12}C^{\pm}$, $^{24}C_2^{\pm}$, $^{36}C_3^{\pm}$, $^{48}C_4^{\pm}$, $^{60}C_5^{\pm}$, etc.) and $^{39}K^+$ and $^{97}HSO_4^-$, and also few relatively weak organic fragments (*m/z* $^{27}C_2H_3^+$, $^{43}C_2H_3O^+$) (Fig. S3e) (Moffet and Prather, 2009). The EC-containing particles mainly originated from coal combustion (Bond et al., 2013) and vehicle emissions (Yang et al., 2017). The presence of $^{97}HSO_4^-$ also indicates the aging of the particles. Dust particles mainly contain mineral ions signals in MS (Fig. S3f), such as *m/z* $^{27}Al^+$, $^{40}Ca^+$, $^{56}CaO^+/Fe^+$, $^{16}O^-$, $^{17}OH^-$, $^{76}SiO^-$, and $^{79}PO_3^-$. Different from other particles, the dust particle has no obvious signal of $^{97}HSO_4^-$ and $^{62}NO_3^-$. This could be explained by the dust being much fresh from the local road/construction fly ash or dust events. The characteristic ions of NaK-SN, metal, and other particles are listed in Table 1 and Fig. S3(g,h,i), respectively. Due to their relatively low contributions (< 3%), their recognition is not discussed in detail.

Text S2. The spatial distribution for the six major particle types

The potential source contribution function (PSCF) model was applied to further identify the spatial distribution of the pollution sources for the six major particle types. For the rich-K and OC particles (Fig. S11), the large fractions in the southwest of Gaomeigu are potentially influenced by biomass burning and traffic emissions, such as the two nearby highways [the Xili Expressway (G0613) and Dali Expressway (G5611)] (Fig. S12). As shown in Fig. S11, the high PSCF values of BB particle are found along Sino-Burmese border and the sampling surroundings. Combined with intensive fire activities (Fig. S13), the emitting of levoglucosan ($^{45}CHO_2^-$, $^{59}C_2H_3O_2^-$, $^{71}C_3H_3O_2^-$, $^{73}C_3HO_3^-$) from biomass burning will decaye or even vanish (Pratt et al., 2011; Li et al., 2014) during the atmospheric aging processes, thus underestimate the contribution of long-distance regional transport. Tian et al (2022) also suggested that BBOA was partly aged at Gaomeigu. A higher PSCF value of Ammonium particles is seen in the cross-border of northern Myanmar than in the center of Gaomeigu, representing more influences by transportation than the local emission. Owing to the low consumption of coal in the southeastern Tibet Plateau (Li et al., 2016), the high PSCF values of EC-aged particles are more likely from the traffic emissions (Fig. S12). Moreover, sporadic high PSCF values of the EC-aged particles are also found in cross-border northern Myanmar, indicating possible influences of biomass burning emissions (Liu et al., 2021). The high PSCF values of Dust particles are observed in the surrounding areas of the southwestern sampling site.

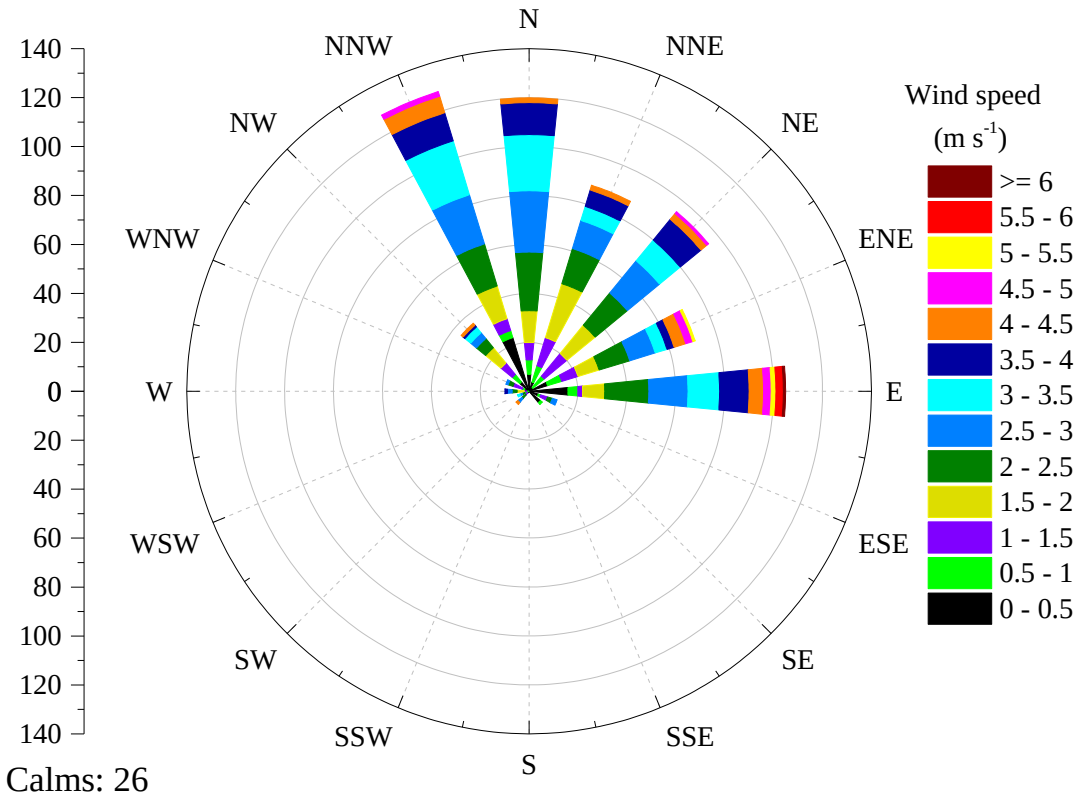

Figure S1. Wind rose of wind direction and wind speed (color bar) during the study period.

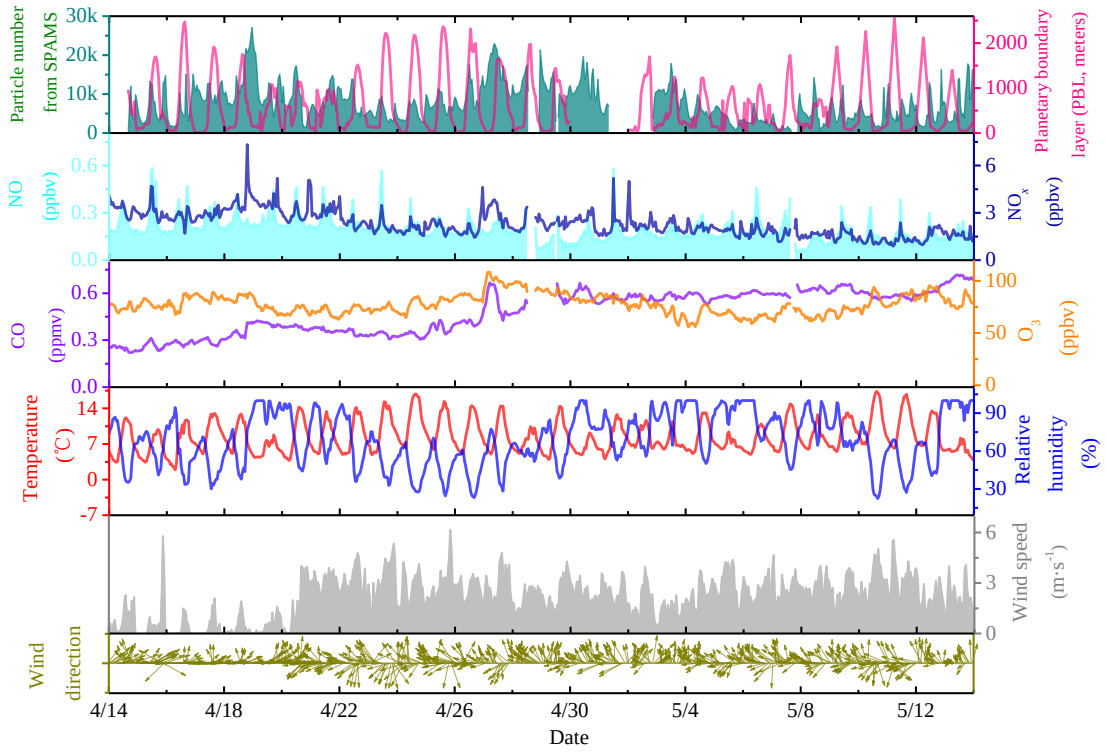

Figure S2. Time series of SPAMS particles, gaseous concentrations (i.e., NO, NO_x, O_3, and CO) and meteorological parameters (planetary boundary layer height, temperature, relative humidity, wind direction, and wind speed).

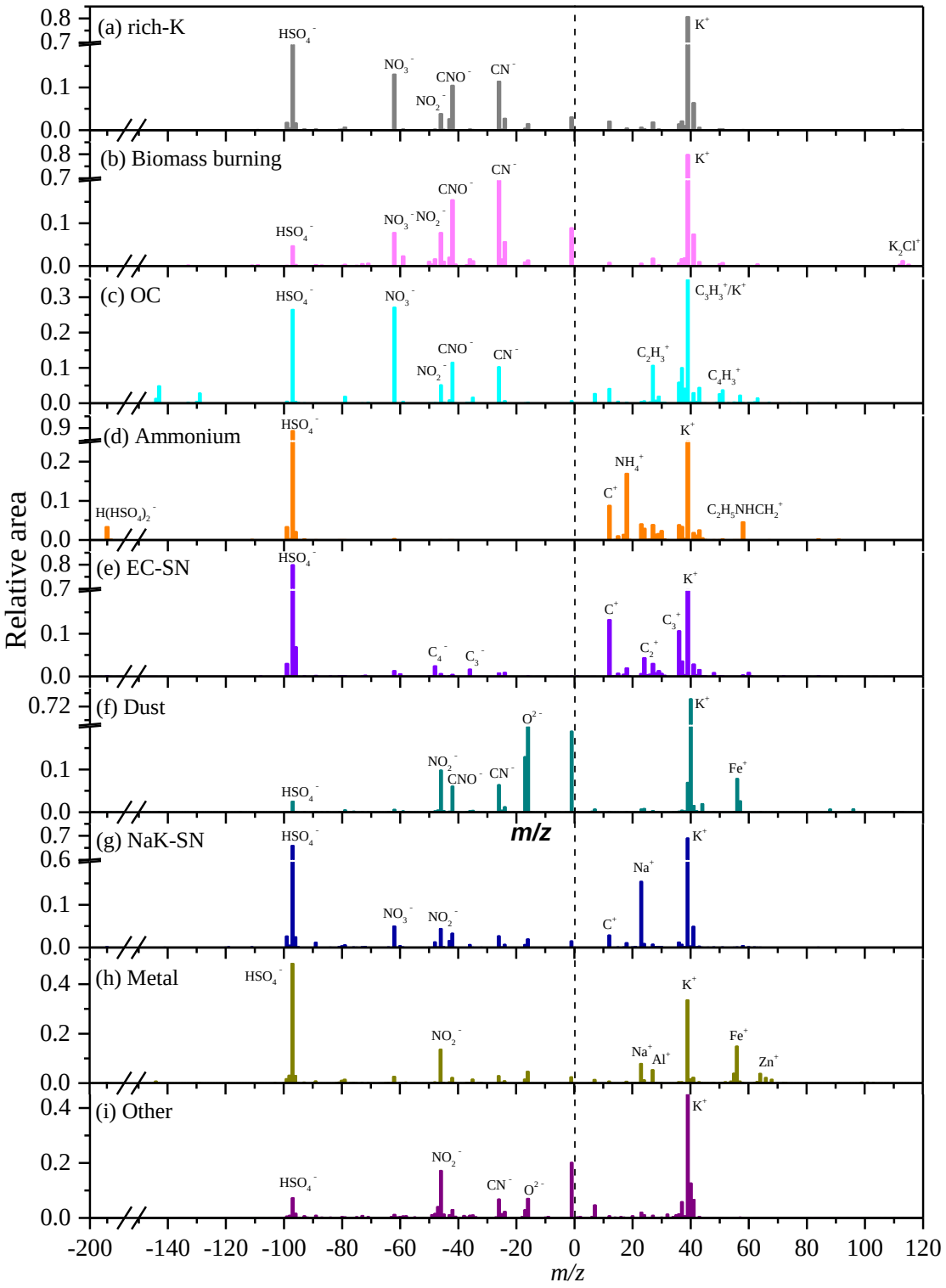

Figure S3. The average mass spectra of the major six particle types: (a) rich-potassium (K), (b) Biomass burning (BB), (c) Organic carbon (OC), (d) Ammonium, (e) Element carbon (EC)-aged, (f) Dust; and the relatively low contributions (< 3%) types of (g) Sodium, Potassium (NaK)-SN, (h) Metal, (i) Other.

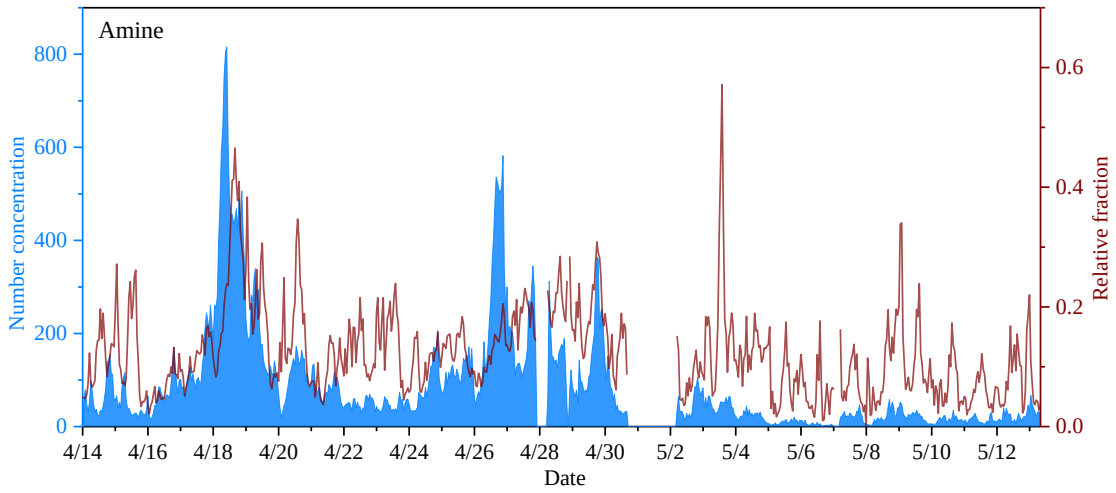

Figure S4. Time-series of the number concentrations (blue area) and the relative fraction (dark red line) of Amine-containing particles during the observation periods.

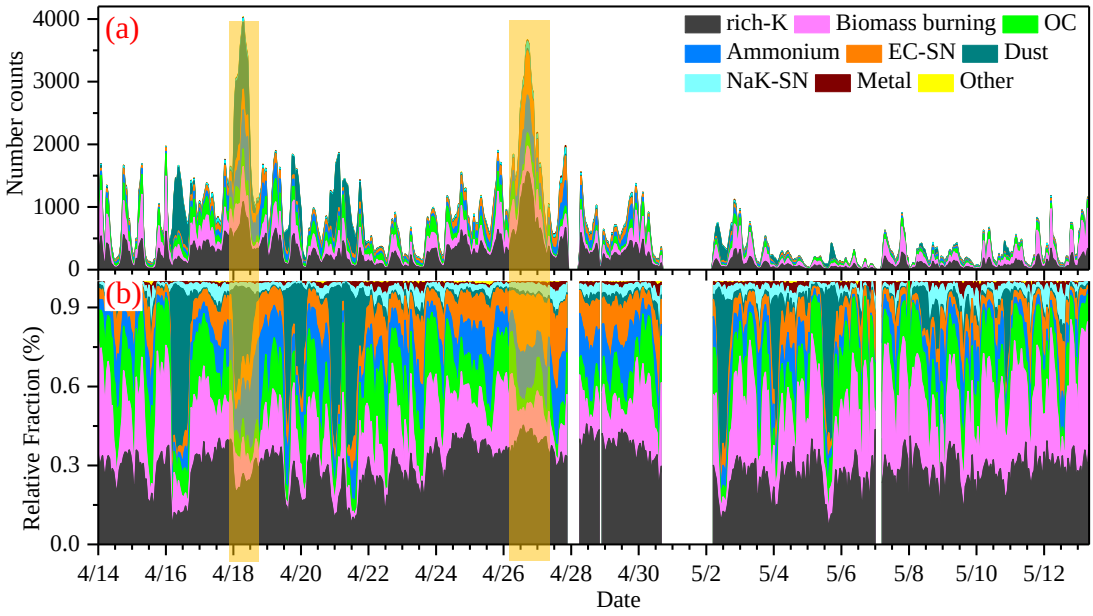

Figure S5. Time-series plots of (a) the number concentrations and (b) the relative fraction of nine particle groups during the observation periods. Particle type abbreviations as in supplementary of section 1. The two yellow shades correspond to Episode Ⅰ and Ⅱ, respectively.

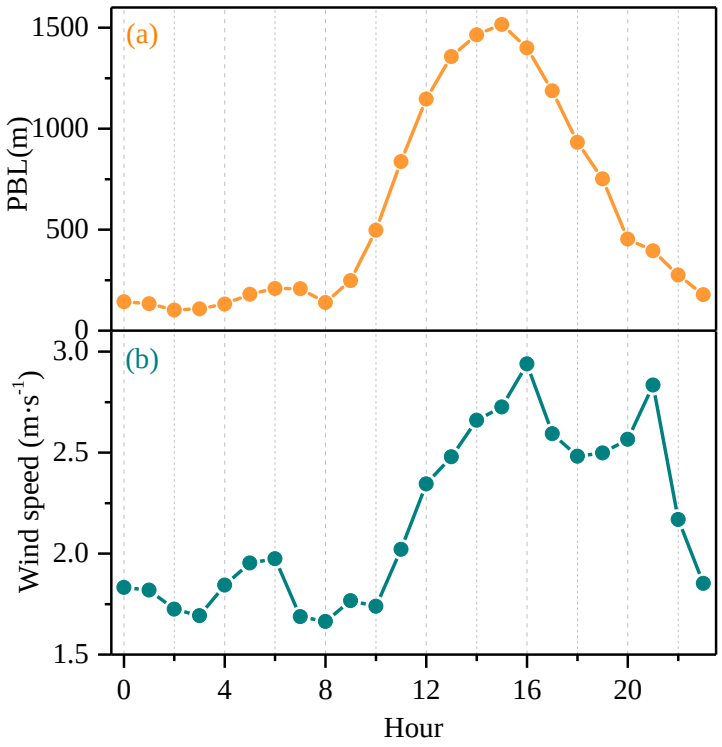

Figure S6. Diurnal variation of the (a) plantary boundary larye (PBL) and (b) wind speed (WS) during entire observation period.

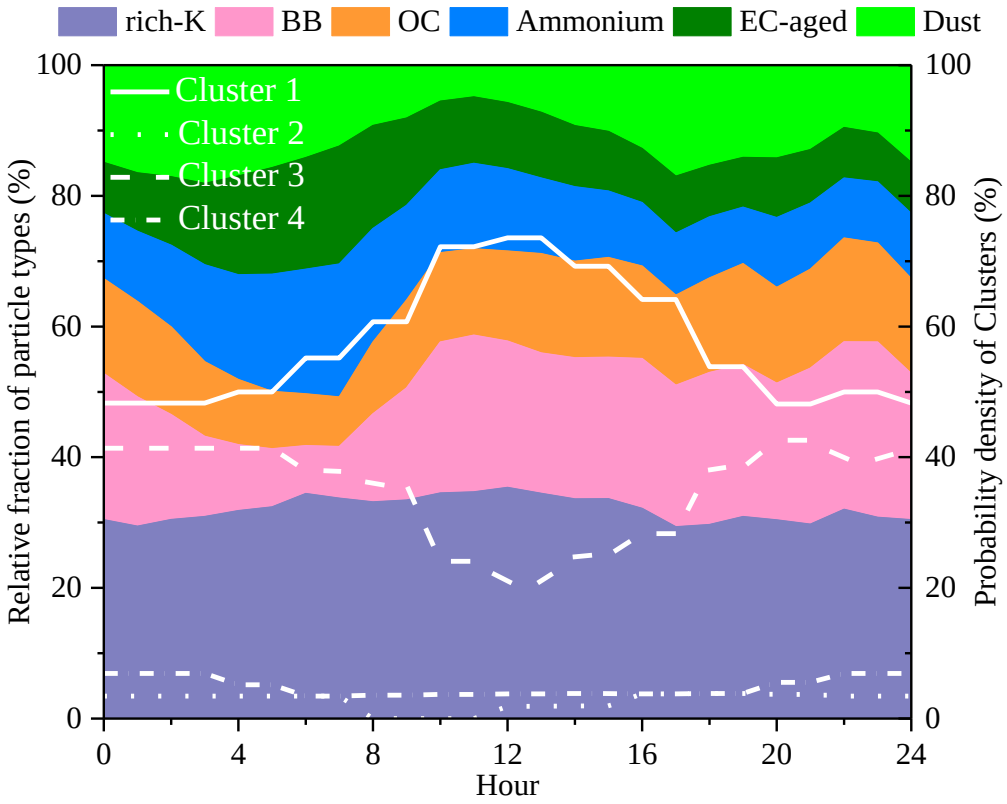

Figure S7. Diurnal variation of the relative fraction of the six major particle types and the probability density of the four clusters during entire observation period. The white lines represent the probability densities for the four air clusters.

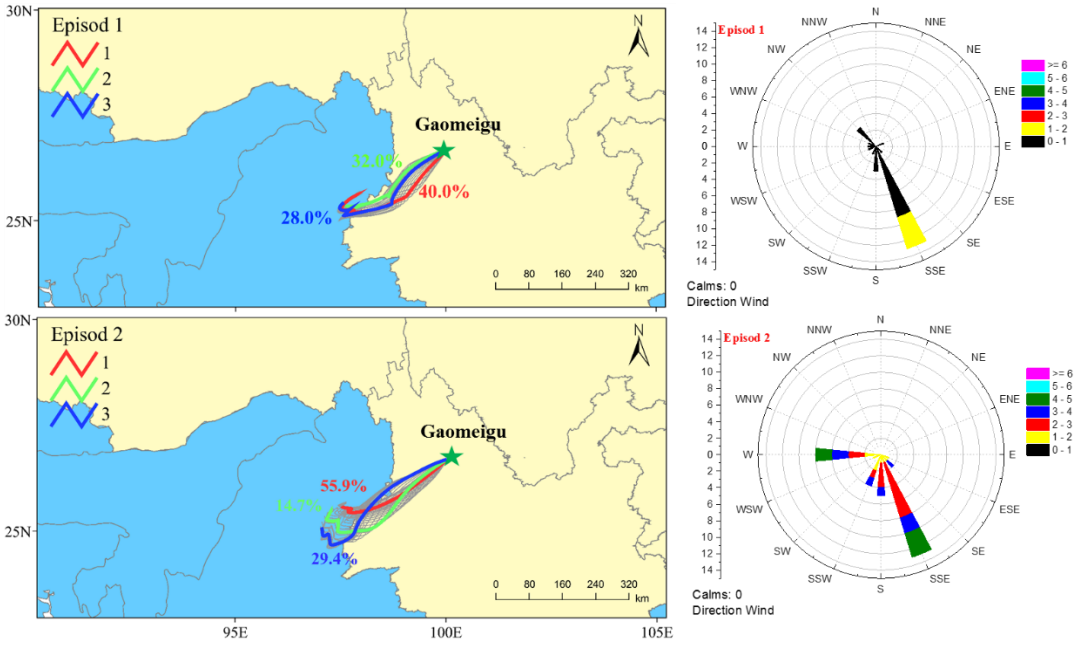

Figure S8. Maps of the mean HYSPLIT back trajectory clusters (72 h) at the height of 500 m during the Episode I (from 08:00 April 18th to 08:00 April 19th 2019) and Episode II (from 17:00 April 26th to 02:00 April 28th), and the wind speed and direction.

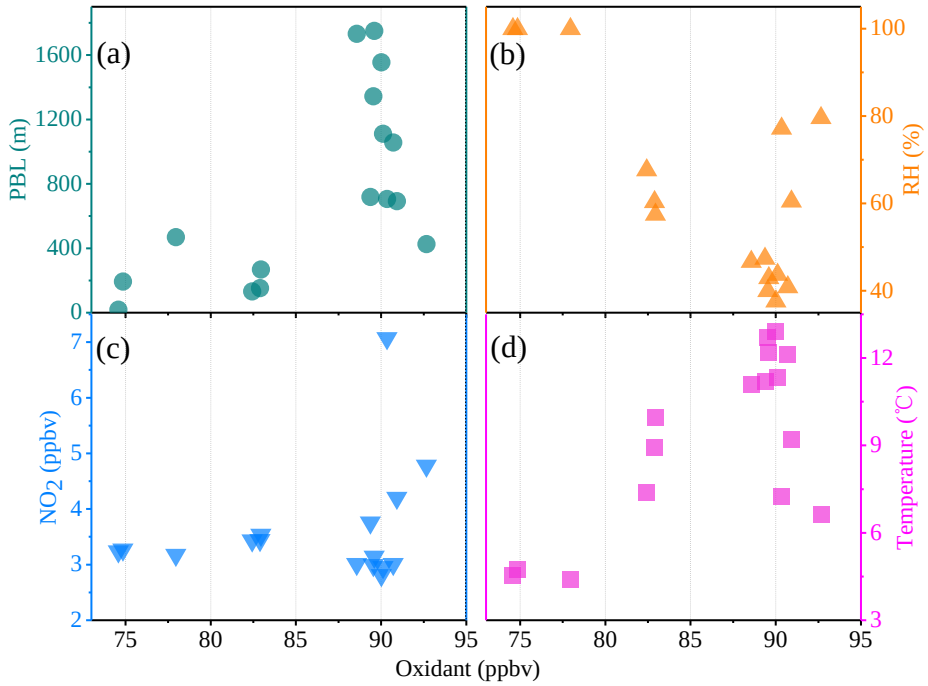

Figure S9. Correlations between oxidant (O_x) concentration and (a) PBL, (b) RH, (c) NO_2 concentration, and (d) temperature during Episode I.

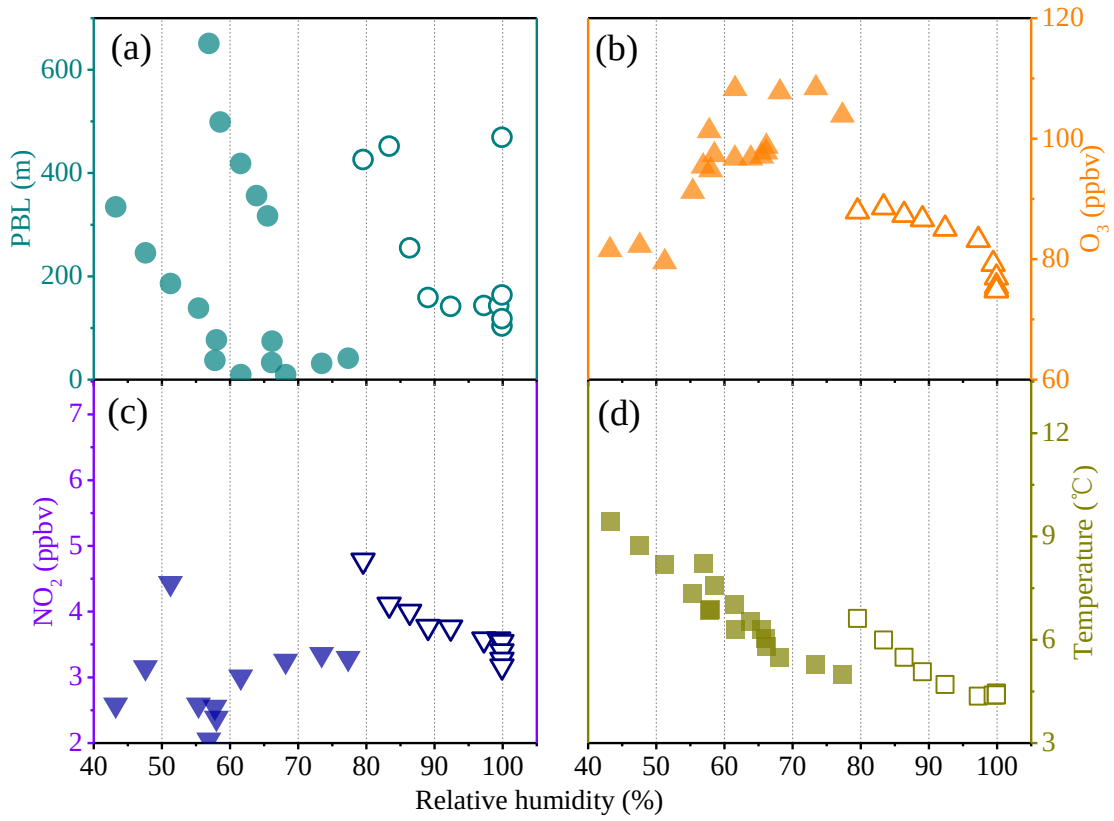

Figure S10. Correlations between RH and (a) PBL height, (b) O_3 concentration, (c) NO_2 concentration, and (d) temperature; the solid shape is during the Episode II, the open shape is during the Episode I.

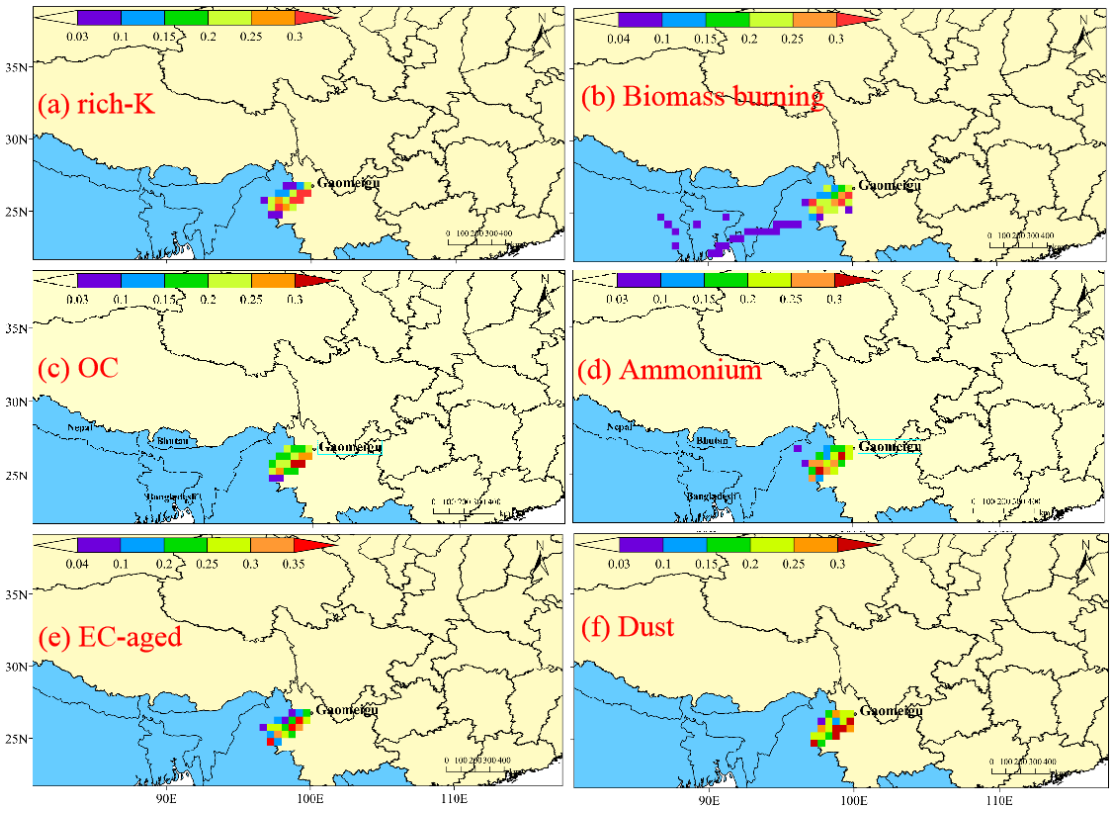

Figure S11. Maps of the potential source contribution functions for (a) rich-K, (b) Biomass burning, (c) OC, (d) Ammonium, (e) EC-aged, and (f) Dust particles; the 75th percentile was 309, 194, 127, 101, 84 and 84, respectively.

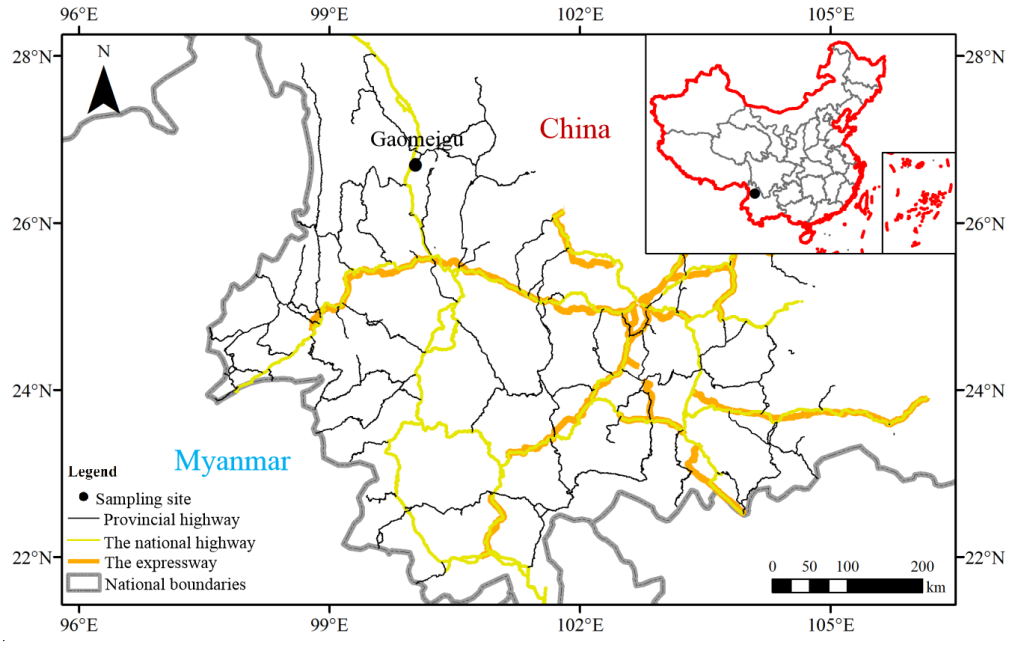

Figure S12. Map of highway distribution near sampling sites from ArcGis10.6 software; dataset acquired from Global Roads Inventory Project (GRIP): global roads database (https://www.globio.info/resources). The GRIP dataset consists of global and regional vector datasets in ESRI filegeodatabase and shapefile format, and global raster datasets of road density at a 5 arcminutes resolution (~8×8km).

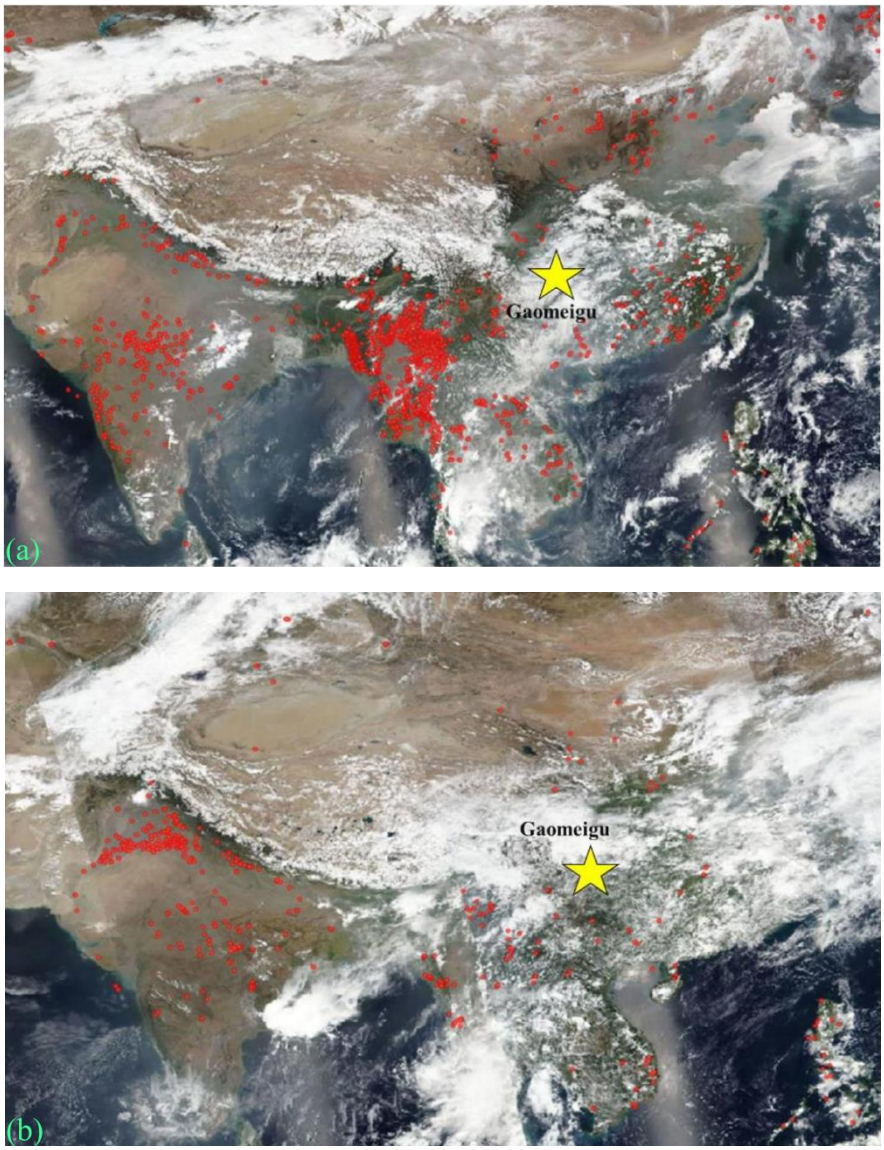

Figure S13. Monthly average fire site maps for (b) April 2018, and (c) May 2018. The fire site maps are from © NASA (National Aeronautics and Space Administration) (https://www.nasa.gov/image-feature/goddard/2018/a-world-on-fire).

Reference

Bi, X.H., Zhang, G.H., Li, L., Wang, X.M., Li, M., Sheng, G.Y., Fu, J.M., Zhou, Z., 2011. Mixing state of biomass burning particles by single particle aerosol mass spectrometer in the urban area of PRD, China, Atmos. Environ., 45, 3447–3453, https://doi.org/10.1016/j.atmosenv.2011.03.034.

Bond, T.C., Doherty, S.J., Fahey, D.W., Forster, P.M., Berntsen, T., DeAngelo, B.J., Flanner, M.G., Ghan, S., Kärcher, B., Koch, D., Kinne, S., Kondo, Y., Quinn, P.K., Sarofim, M.C., Schultz, M.G., Schulz, M., Venkataraman, C., Zhang, H., Zhang, S., Bellouin, N., Guttikunda, S.K., Hopke, P.K., Jacobson, M.Z., Kaiser, J.W., Klimont, Z., Lohmann, U., Schwarz, J.P., Shindell, D., Storelvmo, T., Warren, S.G., and Zender, C.S., 2013. Bounding the role of black carbon in the climate system: a scientific assessment, J. Geophys. Res. Atmos., 118, 5380–5552, https://doi.org/10.1002/jgrd.50171.

Cadle, S.H., Mulawa, P.A., 1980. Low-molecular-weight aliphatic amines in exhaust from catalyst-equipped cars, Environ. Sci. Technol. 14 (6), 718–723, https://doi.org/10.1021/es60166a011.

Cahill, J.F., Suski, K., Seinfeld, J.H., Zaveri, R.A., Prather, K.A., 2012. The mixing state of carbonaceous aerosol particles in northern and southern California measured during CARES and CalNex 2010, Atmos. Chem. Phys., 12, 10989–11002, https://doi.org/10.5194/acp-12-10989-2012.

Hatch, L.E., Creamean, J.M., Ault, A.P., Surratt, J.D., Chan, M.N., Seinfeld, J.H., Edgerton, E.S., Su, Y., Prather, K.A., 2011. Measurements of Isoprene-Derived Organosulfates in Ambient Aerosols by Aerosol Time-of-Flight Mass Spectrometry–Part1: Single Particle Atmospheric Observations in Atlanta, Environ. Sci. Technol., 45, 5105–5111, https://doi.org/10.1021/es103944a.

Lall, R., Thurston, G.D., 2006. Identifying and quantifying transported vs. local sources of new York City $PM_{2.5}$ fine particulate matter air pollution, Atmos Environ., 40, 333–346, https://doi.org/10.1016/j.atmosenv.2006.04.068.

Li, L., Li, M., Huang, Z.X., Gao, W., Nian, H.Q., Fu, Z., Gao, J., Chai, F.H., Zhou, Z., 2014. Ambient particle characterization by single particle aerosol mass spectrometry in an urban area of Beijing, Atmos. Environ. 94, 323–331, https://doi.org/10.1016/j.atmosenv.2014.03.048.

Li, C., Bosch, C., Kang, S., Andersson, A. Chen., P. Zhang, Q., Cong., Z. Chen, B., and Gustafsson., Ö., 2016. Sources of black carbon to the Himalayan–Tibetan Plateau glaciers, Nat. Commun., 7, 12574, https://doi.org/10.1038/ncomms12574.

Lin, Q.H., Zhang, G.H., Peng, L., Bi, X.H., Wang, X.M., Brechtel, F.J., Li, M., Chen, D.H., Peng, P.A., Sheng, G.Y., Zhou, Z., 2017. In situ chemical composition measurement of individual cloud residue particles at a mountain site, southern China, Atmos. Chem. Phys., 17, 8473–8488, https://doi.org/10.5194/acp-17-8473-2017.

Liu, H.K., Wang, Q.Y., Xing, L., Zhang, Y., Zhang, T., Ran, W.K., Cao, J.J., 2021. Measurement report: quantifying source contribution of fossil fuels and biomass-burning black carbon aerosol in the southeastern margin of the Tibetan Plateau, Atmos. Chem. Phys., 21, 973–987, https://doi.org/10.5194/acp-21-973-2021.

Moffet, R.C., Foy, B.D., Molina, L.A., Molina, M.J., Prather, K.A., 2008. Measurement of ambient aerosols in northern Mexico City by single particle mass spectrometry. Atmos. Chem. Phys. 8 (16), 4499–4516, https://doi.org/10.5194/acpd-7-6413-2007.

Moffet, R.C., Prather, K.A., 2009. In-situ measurements of the mixing state and optical properties of soot with implications for radiative forcing estimates, P. Natl. Acad. Sci. USA, 106, 11872–11877, https://doi.org/10.1073/pnas.0900040106.

Pratt, K.A., Murphy, S.M., Subramanian, R., DeMott, P.J., Kok, G. L., Campos, T., Rogers, D.C., Prenni, A.J., Heymsfield, A.J., Seinfeld, J.H., Prather, K.A., 2011. Flight-based chemical characterization of biomass burning aerosols within two prescribed burn smoke plumes, Atmos. Chem. Phys., 11, 12549–12565, https://doi.org/10.5194/acp-11-12549-2011.

Rehbein, P. J., Jeong, C. H., McGuire, M. L., Yao, X., Corbin, J. C., Evans, G. J.,2011. Cloud and fog processing enhanced gas-toparticle partitioning of trimethylamine, Environ. Sci. Technol., 45, 4346–4352, https://doi.org/10.1021/es1042113.

Seinfeld, J.H., Pandis, S.N., 2012. Atmospheric Chemistry and Physics: from Air Pollution to Climate Change, John Wiley & Sons., 1326. https://doi.org/10.1080/00139157.1999.10544295.

Shen, L.J., Wang, H.L., Lü, S., Zhang, X.H., Yuan, J., Tao, S.K., Zhang, G.J., Wang, F., Li, L., 2017. Influence of pollution control on air pollutants and the mixing state of aerosol particles during the 2nd World Internet Conference in Jiaxing, China, J. Clean. Prod., 149, 436–447, https://doi.org/10.1016/j.jclepro.2017.02.114.

Sun, Y.L., Zhang, Q., Schwab, J.J., Yang, T., Ng, N.L., Demerjian, K.L., 2012. Factor analysis of combined organic and inorganic aerosol mass spectra from high resolution aerosol mass spectrometer measurements, Atmos. Chem. Phys., 12, 8537–8551, https://doi.org/10.5194/acp-12-8537-2012.

Xu, L.L., Wu, X., Hong, ZY., Zhang, Y.R., Deng, J.J., Hong, Y.W., Chen, J.S., 2018. Composition, mixing state, and size distribution of single submicron particles during pollution episodes in a coastal city in southeast China, Environ. Sci. Pollut. Res., 26, 1464–1473, https://doi.org/10.1007/s11356-018-3469-x.

Yang, J., Ma, S.X., Gao, B., Li, X.Y., Zhang, Y.J., Cai, J., Li, M., Yao, L.A., Huang, B., Zheng, M., 2017. Single particle mass spectral signatures from vehicle exhaust particles and the source apportionment of on-line $PM_{2.5}$ by single particle aerosol mass spectrometry, Sci. Total Environ. 593, 310–318, https://doi.org/10.1016/j.scitotenv.2017.03.099.

Yang, F., Chen, H., Du, J., Yang, X., Gao, S., Chen, J., Geng, F., 2012. Evolution of the mixing state of fine aerosols during haze events in Shanghai, Atmos. Res. 104, 193–201, https://doi.org/10.1016/j.atmosres.2011.10.005.

Zhang, J.K., Luo, B., Zhang, J.Q., Ouyang, F., Song, H.Y., Liu, P.C., Cao, P., Schäfer, K., Wang, S.G., Huang, X.J., Lin, Y.F., 2017. Analysis of the characteristics of single atmospheric particles in Chengdu using single particle mass spectrometry, Atmos. Environ. 157, 91–100, https://doi.org/10.1016/j.atmosenv.2017.03.012.